Extreme redox variations in a superdeep diamond from a subducted slab

Fabrizio Nestola¹, Margo E. Regier², Robert W. Luth², D. Graham Pearson², Thomas Stachel², Catherine McCammon³, Michelle D. Wenz⁴, Steven D. Jacobsen⁴, Chiara Anzolini², Luca Bindi⁵, Jeffrey W. Harris⁶

6 Department of Geosciences, University of Padova, I-35131 Padova, Italy.

8 ³Bayerisches Geoinstitüt, University of Bayreuth, D-95440 Bayreuth, Germany.

⁵Department of Earth Sciences, University of Firenze, I-50121 Firenze, Italy.

11 ⁶School of Geographical and Earth Sciences, University of Glasgow, G12 8QQ Glasgow, UK.

The introduction of volatile-rich subducting slabs to the mantle may locally generate large redox gradients, affecting phase stability, element partitioning and volatile speciation¹. Here we investigate the redox conditions of the deep mantle recorded in inclusions in a diamond from Kankan, Guinea. Enstatite (former bridgmanite), ferropericlase and a uniquely Mgrich olivine (Mg# 99.9) inclusion indicate formation in highly variable redox conditions near the 660 km seismic discontinuity. We propose a model involving dehydration, rehydration, and dehydration in the underside of a warming slab at the transition zone – lower mantle boundary. Fluid liberated by dehydration in a crumpled slab, driven by heating from the lower mantle, ascends into the cooler interior of the slab, where the H₂O is sequestered in new hydrous minerals. Consequent fractionation of the remaining fluid produces extremely reducing conditions, forming Mg-endmember ringwoodite. This fractionating fluid also precipitates the host diamond. With continued heating, ringwoodite in the slab surrounding the diamond forms bridgmanite + ferropericlase, trapped as the diamond grows in hydrous fluids produced by dehydration of the warming slab.

²Department of Earth and Atmospheric Sciences, University of Alberta, AB T6G 2E3 Edmonton, Canada.

⁴Department of Earth and Planetary Sciences, Northwestern University, Evanston, Illinois 60208, USA.

Superdeep diamonds from >300 km depth act as inert capsules that can transport material to the surface without chemical alteration. The majority of these diamonds are associated with subducted oceanic crust^{2,3}, but others lack the isotopic and elemental signatures characteristic of altered crust and likely originate from the convecting mantle or subducted oceanic peridotites⁴⁻⁶. The Kankan region of Guinea yields both of these distinct sublithospheric diamond populations, with both being characterized by the resorbed shapes and low N contents typical of superdeep diamonds worldwide¹. The subset of diamonds with asthenospheric and transition zone inclusions has stable isotopic characteristics similar to carbonate-rich oceanic crust, while the deeper subset, with an assemblage principally of ferropericlase and MgSiO₃ (primary bridgmanite found as its lowpressure polymorph - enstatite) inclusions, has diamond isotopic signatures reflective of a convecting mantle origin^{1,7-8}. While the origin of the asthenospheric and transition zone diamonds is now strongly tied to melting of carbonated slabs^{3,9}, the origin of the ferropericlase- and MgSiO₃bearing diamonds is still controversial¹⁰. Here, we investigate some extreme chemical anomalies within ferropericlase, olivine and MgSiO₃-inclusions recovered from a super-deep diamond from Kankan, Guinea. The inclusion chemistry confirms that this diamond originates from near the transition zone/lower mantle boundary and reveals the existence of an extremely variable redox environment that may have arisen as a stalled oceanic slab ("megalith") warms to ambient mantle temperatures.

48

49

50

51

52

30

31

32

33

34

35

36

37

38

39

40

41

42

43

44

45

46

47

Inclusion assemblage. Raman spectroscopy and single-crystal X-ray diffraction (SCXRD) identified seven non-touching mineral inclusions within Kankan diamond KK203. Four of these were recovered (the other three were too small) during the diamond breakage and are: olivine, enstatite, ferropericlase and an epigenetic clinopyroxene.

Averaged electron probe microanalyses of these four inclusions after diamond breakage are reported in Table 1. A complete set of analyses for all phases are reported in Supplementary Tables 1 and 2. Enstatite was also analysed by Raman spectroscopy (Extended Data Figure 1). An additionally recovered clinopyroxene inclusion is compositionally inhomogeneous and considered either as contamination or as an epigenetic (altered) inclusion and not considered further here. Unexpectedly, the olivine inclusion is pure forsterite (Mg# 99.9), and currently unique for an olivine inclusion in diamond. Similar inclusion associations to those found in KK203 have been explained either as relics of phase assemblages entrapped at the 660 km transition zone – lower-mantle boundary (ferropericlase + retrogressed ringwoodite + retrogressed bridgmanite)¹², or involving retrogressed ringwoodite as a transient retrograde reaction product of bimineralic ferropericlase + bridgmanite inclusions⁵. With the present assemblage, all three inclusions were not zoned and X-ray microtomography (Extended Data Figure 2) showed no fractures from the inclusions to the diamond surface, indicating the inclusions were neither altered nor late-stage reaction products⁴. While ferropericlase and enstatite are spatially almost in contact within the diamond, the olivine is not. This spatial association may allow for entrapment of the olivine inclusion at a distinct

70

71

72

73

74

53

54

55

56

57

58

59

60

61

62

63

64

65

66

67

68

69

growth stage.

Super-deep origin of diamond KK203. Single-crystal X-ray diffraction performed on diamond KK203 allowed refinement of the unit cell of the forsterite inclusion. 81 collected X-ray reflections (see olivine.tabb reflections file, readable via Crysalis software) gave the following orthorhombic unit-cell values:

75 $a = 4.748 \pm 0.014 \text{ Å}, b = 10.32 \pm 0.03 \text{ Å}, c = 5.806 \pm 0.017 \text{ Å}, V = 284 \pm 1 \text{ Å}^3$

Such a unit-cell volume is extremely small, considering that, at room temperature and pressure, Fogg. should have a volume of $V = 290.57 \text{ Å}^3$ (e.g., with $V = 308.56 - 0.1801 \times \%\text{Fo}$)¹³. A synthetic sample of Fo₁₀₀ studied by [16] has a volume of 291.15 Å³. Thus, olivine in diamond KK203 must be under a very high residual pressure ($P_{\rm inc}$). Lithospheric olivine inclusions in diamond show relatively low residual pressures with $P_{\rm inc}$ between 0.4 to 0.6 GPa^{14,15}. Using the equation of state for mantle olivine¹⁵ and a room pressure and temperature volume of olivine with composition Fo_{99.9} equal to 290.57 Å³, we can calculate a $P_{\rm inc} = 3.0 \pm 0.5$ GPa, or 3.3 ± 0.5 GPa using the volume of [16]. These are the highest residual pressures ever found for an olivine inclusion in diamond. Starting from these $P_{\rm inc}$ estimates, we can determine the minimum pressure of entrapment, $P_{\rm trap}$ (which corresponds to the minimum pressure of diamond formation), using the equation of state of diamond¹⁷ and the EosFit-Pinc software¹⁸. The calculation provides an entrapment pressure P_{trap} = 9.1±0.7 GPa or 9.6±0.7 GPa at 1,400°C, lying on the mantle adiabat^{19,20}. This calculation, however, is based on purely elastic theory and cannot correctly approximate our diamondinclusion couple: diamond KK203 underwent extreme plastic deformation, which can be assessed by comparing the measured unit-cell values with those obtained under hydrostatic compression¹⁶: if we individually measure the residual pressures provided by the a, b and c axes, then we observe extreme differences, with the c axis reaching 14.8 GPa of residual pressure, indicating very strong deviatoric stresses. Diamond can only show such levels of plastic deformation at temperatures \geq 1,600 °C²¹, which are reached only within the deep transition zone where ringwoodite is stable. Thus, we are confident that our anomalous olivine inclusion, characterized by such unusually high residual pressure and deviatoric stress, is a retrogressed ringwoodite. An additional depth constraint comes from the low Al₂O₃ content recorded by the MgSiO₃ inclusion, which is consistent with an origin from just below the 660 km discontinuity (~1 wt% Al₂O₃ for first formed

76

77

78

79

80

81

82

83

84

85

86

87

88

89

90

91

92

93

94

95

96

97

bridgmanite at 660 km depth)²². An origin in metaperidotitic rocks of the deep transition zone and/or shallow lower mantle aligns with the mantle-like signatures of carbon isotopes in diamond KK203 (δ^{13} C: $-3.9\%^{23}$) and oxygen isotopes of its MgSiO₃ inclusion (δ^{18} O: $+5.3\%^{8}$).

The origin of highly magnesian olivine. From the evidence above, we propose that the recovered olivine inclusion in diamond KK203 is a retrogressed low-pressure polymorph of original high-pressure ringwoodite. Such olivine inclusions in superdeep diamonds with inclusions of ferropericlase \pm former bridgmanite \pm former Ca-perovskite have been previously reported from the Rio Soriso, Rio São Luiz and the Juina-5 pipe in Brazil, Kankan in Guinea, and the Panda and DO27 pipes at Lac de Gras, Canada²⁴⁻²⁷. Our olivine (retrogressed ringwoodite) inclusion, however, shows an extreme Mg#, which may relate to three possible environments: (a) subduction of serpentinite, (b) extremely oxidizing conditions, and (c) extremely reducing conditions. Evaluating these three options;

(a) Oxygen (MgSiO₃ inclusion) isotope measurements of our lower mantle sample indicate convecting mantle-like signatures^{8,23}, and lack evidence for a seawater exchange expected from a serpentinite protolith²⁸. In addition, olivines formed from serpentinite protoliths via dehydration often have elevated MnO contents²⁹, which is inconsistent with the low concentrations of <0.1 wt.% MnO in our sample. A serpentinite protolith for the Mg#-rich olivine in KK203 is, therefore, considered highly unlikely.

(b) An alternative environment for producing extreme Mg#s in olivine is within subaerial lava flows, where conditions can be extremely oxidizing. Olivine cannot incorporate ferric iron without

distorting its crystal structure, so highly oxidizing conditions will either cause fayalite to break down to laihunite (deformed olivine) and magnetite³⁰, or to coexist with hematite³¹. While these reactions can produce highly magnesian residual olivine (reported Mg#s \leq 99.8), they have only been observed at surficial conditions³¹. However, the extremely low NiO (close to the detection limit) of our forsterite inclusion cannot be explained by oxidation, as highly magnesian olivines reported from oxidized lavas have equivalent NiO contents to those of lower Mg# olivines from unoxidized portions of the same flows³¹.

(c) Instead, we attribute the inverse relationship between high olivine Mg# and low NiO to equilibration with FeNi alloys or melts at f_{02} conditions more reducing than the iron-wüstite (IW) buffer³². The production of silicate minerals with extreme Mg# (99.3-99.8) has been demonstrated in multiple highly-reducing experiments that involve SiC or metal phases^{33,34}. In fact, previous workers³⁴ predicted that nearly pure Mg-silicates would be an indicator of extremely reducing conditions, 3 - 6 log units f_{02} lower than IW. This is much lower than estimates of the f_{02} of the ambient deep mantle, which would be ~1.5 log units below the IW buffer, based on equilibrium between FeNi metal and an assumed bulk mantle Mg# of ~90³⁵.

Diamond formation model. Although the highly magnesian olivine in KK203 is indicative of extremely reducing conditions, neither the other inclusions in KK203, nor inclusions from other diamonds derived from near the 660 km discontinuity, are extremely magnesian. Indeed, the majority of the ferropericlase inclusions in Kankan diamonds have high NiO contents, which are consistent with lower mantle f_{O2} conditions slightly above FeNi metal saturation³⁶. These estimates are supported by previous Mossbauer measurements of lower mantle ferropericlase from Kankan,

some of which have indicated f_{02} conditions approaching the upper limit of diamond stability (\leq 4.3 log units above IW)^{37,38}. Mössbauer spectra collected on the ferropericlase inclusion in KK203 show negligible Fe³⁺/ Σ Fe, indicating f_{02} conditions near the IW buffer (Fig. 1, Extended Data Table 1). Thus, considering the full suite of lower mantle diamonds at Kankan, we propose that the mantle environment near the transition zone/lower mantle boundary sampled by this diamond suite must locally vary in oxygen fugacity by about 8-10 log units, from Δ log f_{02} (IW) \sim +4 (typical Kankan diamonds) to \sim -4 to -6.7 (KK203 diamond). We propose that such extreme variability can be produced in a subducted, warming slab at the transition zone – lower mantle boundary³⁹, and that the inclusions in KK203 represent two stages of diamond growth.

154 The extremely Mg-rich ringwoodite forms by reaction of the Fe₂SiO₄ component, sequestering the

155 Fe into metal via the reaction:

156
$$Fe_2SiO_4 = 2 Fe + SiO_2 + O_2$$
 Eq. 1

under extremely reducing conditions³⁴. Depending on the assumed composition of metal (or metal melt) and the activity of silica, we calculate the Mg# of the ringwoodite reaches 99.9 at -4 to -6.7 log units below IW (see Supplementary Table 3 for details). If ambient mantle is only 1.5 log units below IW, how do the required ultra-reducing conditions form? Previous authors³⁴ proposed such reducing conditions can result from extreme fractionation of an H₂O-rich C-H-O fluid that initially is slightly more reduced than a water-maximum composition. In their model, H₂O removal from the fluid by formation of hydrous minerals drives the residual fluid toward the C-H side-line in the C-H-O system while also precipitating C. We propose that the introduction of lithospheric slabs into the deep mantle can create the necessary conditions for similar fractionation at the transition zone – lower mantle region. Subducting slabs can transport H₂O in hydrous phases to the transition zone³⁹, where they can stall and form "megaliths"^{11,40}. Warming of the stalled megalith by the

surrounding mantle will cause it to dehydrate. Previous attention has focused on the upper slab-mantle interface, where the H₂O liberated by dehydration in the slab ascends into the overlying, hotter mantle, in which hydrous phases are unlikely to be stable. However, if the slab buckles upon reaching the transition zone – lower mantle region as suggested by geophysical modelling⁴¹, then the hydrated upper section of the slab will be inverted and in contact with the lower mantle, which will heat the slab from below. Dehydration of that region of the slab will release fluid that escapes upwards into the cooler interior of the slab, whereupon hydrous DHMS phases – and possibly hydrous ringwoodite⁴² – will form, removing H₂O from the fluid to drive the necessary fractionation of the fluid to very reducing conditions. This inner portion of the slab, that remained comparatively cool as the slab was subducting, would not have been fully hydrated during subduction and therefore would act as a sponge, soaking up H₂O. Any metal formed by pressure-induced disproportionation in the fluid's path would also react via:

180 2Fe (mantle) +
$$H_2O$$
 (slab) = FeO + Fe H_x + $(1-x/2)H_2$ Eq. 2^{43}

181 FeH_x (mantle) + H₂O (slab) = FeO +
$$(1+x/2)$$
H₂ Eq. 3⁴³

The liberation of H₂ will shift the fluid H:O ratio above two, as well as release any C dissolved in the metal into the fluid. Sequestration of H₂O into hydrous phases drives the residual fluid towards the C-H side-line³⁴, shifting the local f_{02} to values much lower than IW. This fluid would react with ringwoodite of normal Mg# (~90) by reaction 1 above to produce a nearly Fe-free ringwoodite as well as ~7 wt.% metal. The O₂ produced in this reaction would react with CH₄ or H₂ in the fluid to form more H₂O, in turn forming more hydrous phases, reinforcing the fractionation of the fluid back to the C-H side-line. Reaction with CH₄ would also precipitate C, adding to the C produced as the fluid fractionated by removal of H₂O by formation of hydrous phases³⁴. The carbon may initially dissolve into the metal formed by ringwoodite reduction, but with continued supply of

fluid from below, the excess C could precipitate as diamond, entrapping the Mg# 99.9 ringwoodite (Stage 1 in Fig.s 2 and 3). This extreme composition must be isolated quickly by diamond growth to prevent re-equilibration by ambient mantle that had not been exposed to the hyper-reduced fluid. The highly fractionated CH₄-H₂-rich fluid will react with Fe²⁺-bearing silicates or ferropericlase to form metal $+ H_2O \pm C$ as it continues to ascend, returning the local environment to ambient mantle conditions buffered by metal – silicate equilibria. The ferropericlase and bridgmanite are trapped in a second stage of diamond growth (Stage 2, Fig.s 2 and 3) as the diamond sits in a matrix of hydrous metaperidotite and metal near the bottom of the megalith, floating in the lower mantle¹¹, consistent with seismic imaging⁴⁴. Because of the negative Clapeyron slope of the ringwoodite to bridgmanite + ferropericlase transition, this cool megalith region, however, still resides in the ringwoodite stability field. Over time, as this part of the megalith continues to warm, the ringwoodite breakdown reaction sweeps inwards (upwards into the slab), transforming the metaperidotite surrounding the diamond to a lower-mantle assemblage (bridgmanite + ferropericlase), as well as destabilizing the remaining hydrous phases (Fig. 3). The associated densification of the megalith means that more material moves into the bridgmanite + ferropericlase field by isostatic adjustment. The dehydration attending the heating

209

208

191

192

193

194

195

196

197

198

199

200

201

202

203

204

205

206

207

metal (or metal melt), the dominant host for carbon in low-C mantle¹⁰:

211

212

213

The methane produced in Eq. 4 could facilitate the crystallization of diamond if an appropriate oxidizing agent is present³⁹. Recent work has suggested that mantle plumes could provide such an

of the slab will release a hydrous diamond-forming fluid^{39,45}, which could react with C-bearing

oxidizing source⁴⁶. Alternatively, the Fe₂O₃-bearing bridgmanite in the slab could be the oxidizing source via:

217
$$2Fe_2O_3 + CH_4 = 4FeO + C + 2H_2O$$
 Eq. 5

where the FeO produced could be a constituent of ferropericlase or bridgmanite.

Implications. Our mineral assemblage tracks the evolution of the mantle in which diamond KK203 was formed. We suggest that the presence of a pure forsterite end-member olivine inclusion implies that localized environments of the transition zone – lower mantle region can be very reducing and metal-rich, albeit possibly only representing the immediate surroundings of fluid conduits. Such extreme compositions are only likely to be preserved from re-equilibration when encapsulated into robust and chemically inert diamond hosts.

The dichotomy between a reduced, highly magnesian olivine polymorph and more oxidized and/or hydrous superdeep inclusions [ferropericlase⁴⁷, majorite⁴⁸, and ringwoodite⁴²] reflects extreme variations in f_{02} over time in the same location in the deep mantle, as a result of the warming of deeply subducted, hydrated slabs. Given the strong influence of mantle f_{02} on mantle solidi and carbon mobility, these extreme fluctuations and their associated local volatile enhancement are one possible driving force for the production of deeply derived, low-melt fraction magmas such as kimberlites. Further constraining the scale and magnitude of deep mantle f_{02} fluctuations is clearly important to understand these issues.

Competing Interests: The authors declare no competing financial interests.

239240

241

238

242243 References

243244

245

246

1. Palot, M., Pearson, D. G., Stern, R. A., Stachel, T. & Harris, J. W. Isotopic constraints on the nature and circulation of deep mantle C–H–O–N fluids: carbon and nitrogen systematics within ultra-deep diamonds from Kankan (Guinea). *Geochim. Cosmochim. Acta* **139**, 26–46 (2014).

247248

2. Stachel, T. Diamonds from the asthenosphere and the transition zone. *Eur. J. Miner.* 13, 883–892 (2001).

251

3. Walter, M.J., Bulanova, G.P., Armstrong, L.S., Keshav, S., Blundy, J.D., Gudfinnsson, G., Lord,
O.T., Lennie, A.R., Clark, S.M., Smith, C.B., Gobbo, L. Primary carbonatite melt from deeply
subducted oceanic crust. *Nature* 454, 622-625 (2008).

255

4. Harte, B., Harris, J.W., Hutchison, M.T., Watt, G.R., Wilding, M.C., 1999. Lower mantle mineral associations in diamonds from Sao Luiz, Brazil, in: Fei, Y., Bertka, C.M., Mysen, B.O. (Eds.), Mantle Petrology: Field Observations and High Pressure Experimentation: A tribute to Francis R. (Joe) Boyd. The Geochemical Society, Houston, pp. 125-153.

260

5. Stachel, T., Harris, J. W., Brey, G. P. & Joswig, W. Kankan diamonds (Guinea) II: lower mantle
inclusion parageneses. *Contrib. Mineral. Petrol.* 140, 16–27 (2000).

263

6. Smith, E. M. et al. Blue boron-bearing diamonds from Earth's lower mantle. *Nature* 560, 84–87 (2018).

266

7. Stachel, T., Harris, J. W., Aulbach, S. & Deines, P. Kankan diamonds (Guinea) III: δ¹³C and nitrogen characteristics of deep diamonds. *Contrib. Mineral. Petrol.* 142, 465–475 (2002).

269

8. Regier, M. E. et al. The lithospheric-to-lower-mantle carbon cycle recorded in superdeep diamonds. *Nature* **585**, 234–238 (2020).

272

9. Thomson, A.R., Walter, M.J., Kohn, S.C. & Brooker, R.A. Slab melting as a barrier to deep carbon subduction. *Nature* **529**, 76–79 (2016).

275

10. Dasgupta, R. & Hirschmann, M. M. The deep carbon cycle and melting in Earth's interior.
 Earth Planet. Sci. Lett. 298, 1–13 (2010).

278

11. Ringwood, A.E. Phase Transformations and Differentiation in Subducted Lithosphere:
 Implications for Mantle Dynamics, Basalt Petrogenesis, and Crustal Evolution. J. Geol. 90, 611-643 (1982).

- 12. Brey, G. P., Bulatov, V., Girnis, A., Harris, J. W. & Stachel, T. Ferropericlase—a lower mantle phase in the upper mantle. *Lithos* 77, 655–663 (2004).
- 13. Nestola, F. et al. New accurate elastic parameters for the forsterite-fayalite solid solution. Am.
 287 Mineral. 96, 1742-1747 (2011a).
- 14. Nestola, F., Nimis, P., Ziberna, L., Longo, M., Marzoli, A., Harris, J. W., Manghnani, M. H.
 & Fedortchouk, Y. First crystal structure determination of olivine in diamond: composition and implications for provenance in the Earth's mantle. *Earth Planet Sci Lett* 305, 249–255 (2011b).
- 15. Angel, R. J., Alvaro, M. & Nestola, F. 40 years of mineral elasticity: a critical review and a new parameterisation of equations of state for mantle olivines and diamond inclusions. *Phys. Chem. Mineral.* 45, 95–113 (2018).
- 16. Poe, B.T., Romano, C., Nestola, F., & Smyth, J.R. Electrical conductivity anisotropy of dry
 and hydrous olivine at 8 GPa. *Phys. Earth Planet. In.* 181, 103-111 (2010).
- 17. Angel, R. J., Alvaro, M., Nestola, F. & Mazzucchelli, M. L. Diamond thermoelastic properties
 and implications for determining the pressure of formation of diamond–inclusion systems. *Russian Geol. Geophys.* 56, 211–220 (2015).
 303
- 18. Angel, R. J., Mazzucchelli, M. L., Alvaro, M. & Nestola, F. EosFit-Pinc: A simple GUI for host–inclusion elastic thermobarometry. *Am. Mineral.* **102**, 1957–1960 (2017).
- 19. Katsura, T., Yoneda, A., Yamazaki, D., Yoshino, T. & Ito, E. Adiabatic temperature profile in the mantle. *Phys. Earth Planet. Int.* **183**, 212–218 (2010).
- 20. Hasterok, D. & Chapman, D. S. Heat production and geotherms for the continental lithosphere.
 Earth Planet. Sci. Lett. 307, 59–70 (2011).
- 21. Cayzer, N.J., Odake, S., Harte, B., & Kagi, H., Plastic deformation of lower mantle diamonds by inclusion phase transformations: *Eur. J. Mineral.*, 20, 333–339 (2008).
- 22. Wood, B. J. Phase transformations and partitioning relations in peridotite under lower mantle conditions. *Earth Planet. Sci. Lett.* **174**, 341-354 (2000).
- 23. Palot, M., Pearson, D.G., Stern, R.A., Stachel, T. & Harris, J.W. Isotopic constraints on the
 nature and circulation of deep mantle C-H-O-N fluids: Carbon and nitrogen systematics within
 ultra-deep diamonds from Kankan (Guinea). *Geochim. Cosmochim. Ac.* 139, 26-46 (2014).
- 24. Davies, R. M., Griffin, W. L., O'Reilly, S. Y. & Doyle, B. J. Mineral inclusions and
 geochemical characteristics of microdiamonds from the DO27, A154, A21, A418, DO18, DD17
 and Ranch Lake kimberlites at Lac de Gras, Slave Craton, Canada. *Lithos* 77, 39–55 (2004).
- 25. Kaminsky, F. V. et al. Superdeep diamonds from the Juina area, Mato Grosso State, Brazil.
 328 Contrib. Miner. Pet. 140, 734–753 (2001).

288

292

296

309

312

318

322

26. Tappert, R., Stachel, T., Harris, J. W., Shimizu, N. & Brey, G. P. Mineral inclusions in diamonds from the Panda kimberlite, Slave province, Canada. *Eur. J. Miner.* 17, 423–440 (2005).

332

27. Hayman, P. C., Kopylova, M. G. & Kaminsky, F. V. Lower mantle diamonds from Rio Soriso (Juina area, Mato Grosso, Brazil). *Contrib. Miner. Pet.* **149**, 430–445 (2005).

335

28. Regier, M. E. et al. An oxygen isotope test for the origin of Archean mantle roots. *Geochemical Perspect. Lett.* **9**, 6–10 (2018).

338

29. Vance, J. A. & Dungan, M. A. Formation of peridotites by deserpentinization in the Darrington
 and Sultan areas, Cascade Mountains, Washington. *Bull. Geol. Soc. Am.* 88, 1497–1508 (1977).

341

30. Kitamura, M., Shen, B., Banno, S. & Morimoto, N. Fine textures of laihunite, a nonstoichiometric distorted olivine- type mineral. *Am. Mineral.* **69**, 154–160 (1984).

344

31. Blondes, M. S., Brandon, M. T., Reiners, P. W., Page, F. Z. & Kita, N. T. Generation of forsteritic olivine (Fo99·8) by subsolidus oxidation in basaltic flows. *J. Petrol.* **53**, 971–984 (2012).

347

348 32. Frost, D. J. & McCammon, C. A. The Redox State of Earth's Mantle. *Annu. Rev. Earth Planet.* 349 *Sci.* 36, 389–420 (2008).

350

33. Shahar, A. et al. High-temperature Si isotope fractionation between iron metal and silicate. 352 *Geochim. Cosmochim. Acta* **75**, 7688–7697 (2011).

353

34. Schmidt, M. W., Gao, C., Golubkova, A., Rohrbach, A. & Connolly, J. A. Natural moissanite
 (SiC) – a low temperature mineral formed from highly fractionated ultra-reducing COH-fluids.
 Prog. Earth Planet. Sci. 1, 27 (2014).

357

35. Rohrbach, A. & Schmidt, M. W. Redox freezing and melting in the Earth's deep mantle resulting from carbon–iron redox coupling. *Nature* **472**, 209-212 (2011).

360

36. Ryabchikov, I. D. & Kaminsky, F. V. Oxygen potential of diamond formation in the lower mantle. *Geol. Ore Depos.* 55, 1–12 (2013).

363

364 37. McCammon, C. A., Stachel, T. & Harris, J. W. Iron oxidation state in lower mantle mineral assemblages II. Inclusions in diamonds from Kankan, Guinea. *Earth Planet. Sci. Lett.* 222, 423–434 (2004).

367

38. Otsuka, K., Longo, M., McCammon, C. A. & Karato, S. Ferric iron content of ferropericlase as a function of composition, oxygen fugacity, temperature and pressure: Implications for redox conditions during diamond formation in the lower mantle. *Earth Planet. Sci. Lett.* **365**, 7–16 (2013).

- 39. Shirey, S. B., Wagner, L. S., Walter, M. J., Pearson, D. G. & van Keken, P. E. Slab transport
- of fluids to deep focus earthquake depths thermal modeling constraints and evidence from
- 374 diamonds. *AGU Adv.* **2**, e2020AV000304 (2021).

40. Van der Hist, R., Engdahl, R., Spakman, W. & Nolet, G. Tomographic imaging of subducted lithosphere below northwest Pacific island arcs. *Nature* **353**, 37–43 (1991).

41. Billen, M.I. Deep slab seismicity limited by rate of deformation in the transition zone. *Sci. Adv.*6, eaaz7692 (2020).

42. Pearson, D. G. *et al.* Hydrous mantle transition zone indicated by ringwoodite included within diamond. *Nature* **507**, 221–4 (2014).

385 43. Zhu, F., Li, J., Liu, J., Dong, J. & Liu, Z. Metallic iron limits silicate hydration in Earth's transition zone. *Proc. Natl. Acad. Sci.* **116**, 22526–22530 (2019).

388 44. Van der Meer, D.G., van Hinsbergen, D.J.J. & Spakman, W. Atlas of the underworld: Slab
 389 remnants in the mantle, their sinking history, and a new outlook on lower mantle viscosity.
 390 Tectonophysics 723, 309–448 (2018).

45. Harte, B. Diamond formation in the deep mantle: the record of mineral inclusions and their distribution in relation to mantle dehydration zones. *Miner. Mag.* 74, 189–215 (2010).

395 46. Moussallam, Y. et al. Mantle plumes are oxidised. Earth Planet. Sci. Lett. 527, 115798 (2019).

47. Kaminsky, F. V. et al. Oxidation potential in the Earth's lower mantle as recorded by ferropericlase inclusions in diamond. *Earth Planet. Sci. Lett.* **417**, 49–56 (2015).

48. Kiseeva, E. S. et al. Oxidized iron in garnets from the mantle transition zone. *Nat. Geosci.* 11, 401 144–147 (2018).

49. Kawamoto, T. Hydrous phase stability and partial melt chemistry in H2O-saturated KLB-1 peridotite up to the uppermost lower mantle conditions. *Physics of the Earth and Planetary Interiors* **143**, 387–395 (2004).

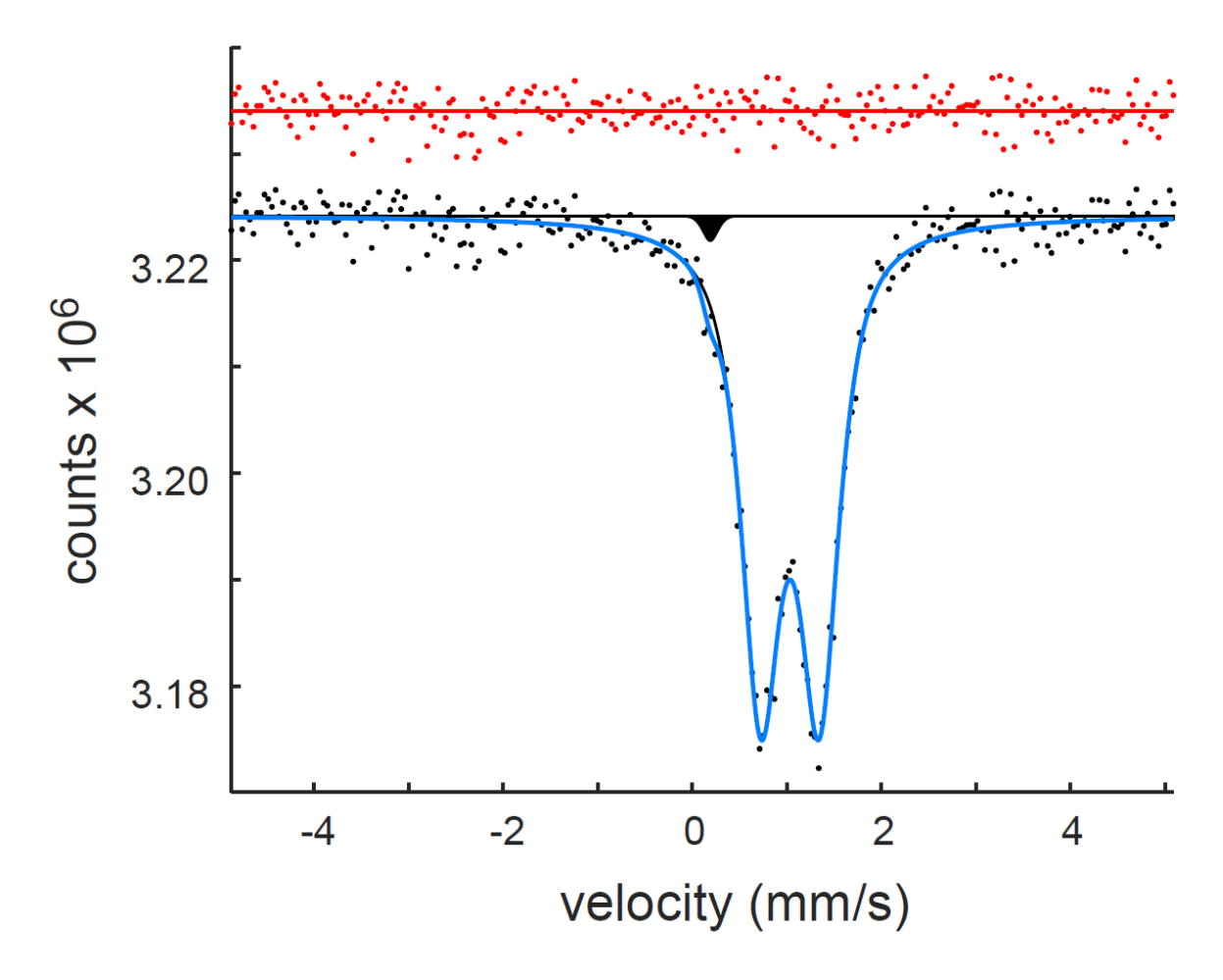


Figure 1: Room temperature Mössbauer spectrum of the ferropericlase inclusion in diamond KK203 showing that its Fe³⁺/ Σ Fe is negligible and indicating f_{02} conditions near the IW buffer. The spectrum was fit to one pseudo-Voigt doublet assigned to Fe²⁺ (unshaded) and one pseudo-Voigt singlet assigned to Fe³⁺ (shaded black). Fe³⁺/ Σ Fe was determined to be 0.01(1) based on relative areas. The inclusion has approximate dimensions $200 \times 200 \times 100 \ \mu \text{m}^3$.

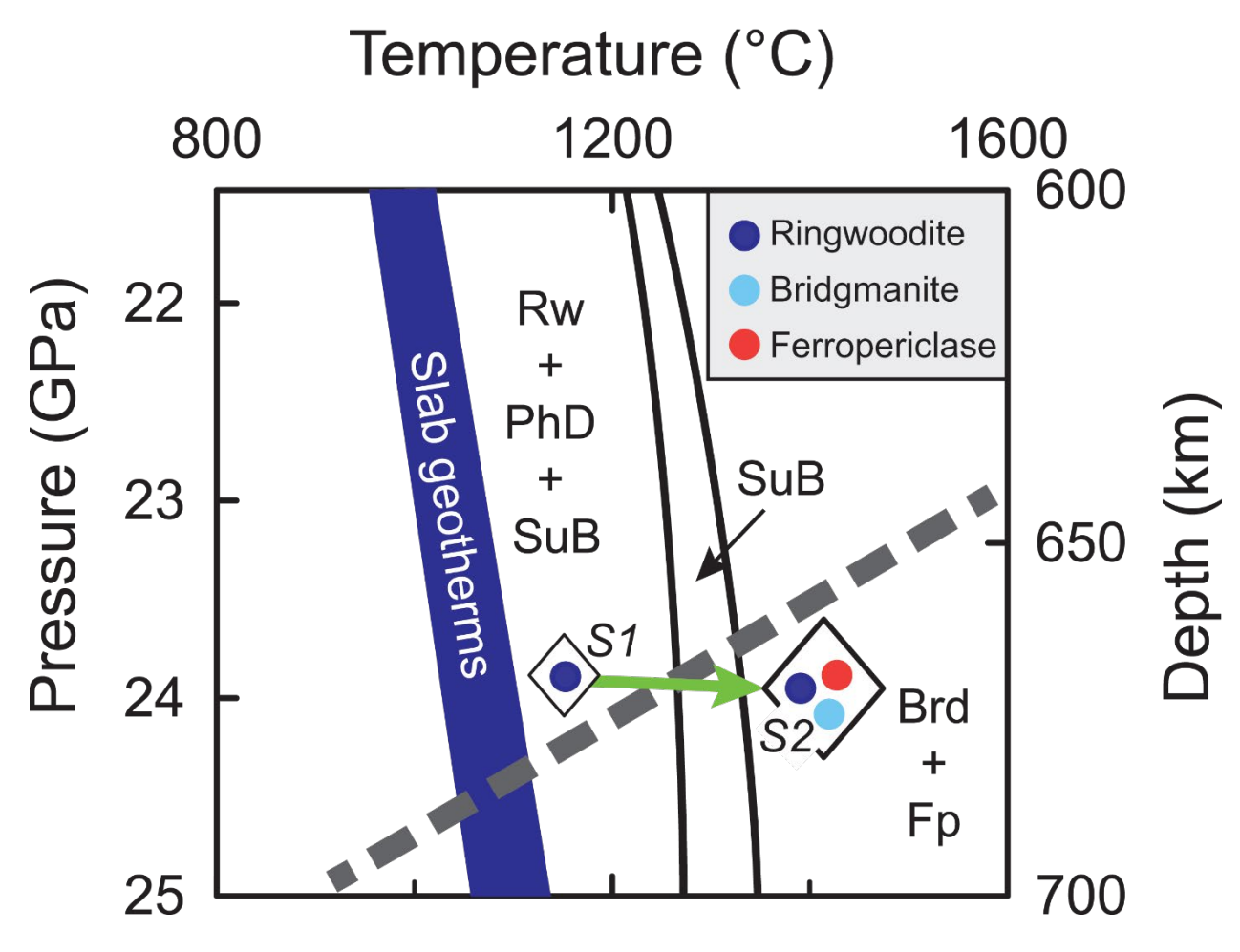


Figure 2: Schematic pressure-temperature plot illustrating processes in a warming hydrated subducted slab over time and the relationships between ringwoodite, ferropericlase and bridgmanite. Green arrow shows heating path experienced by KK203 as slab warms towards ambient mantle temperatures. Gray dashed line is the ringwoodite = bridgmanite + ferropericlase reaction. SI= Stage 1: capture of high-Mg ringwoodite by growing diamond. S2 = Stage 2: encapsulation of bridgmanite and ferropericlase in second stage of diamond growth. Slab geotherms are after [39] and phase relations after [49]. Rw = ringwoodite, PhD = Phase D, SuB = Superhydrous Phase B, Brd = bridgmanite, Fp = ferropericlase.

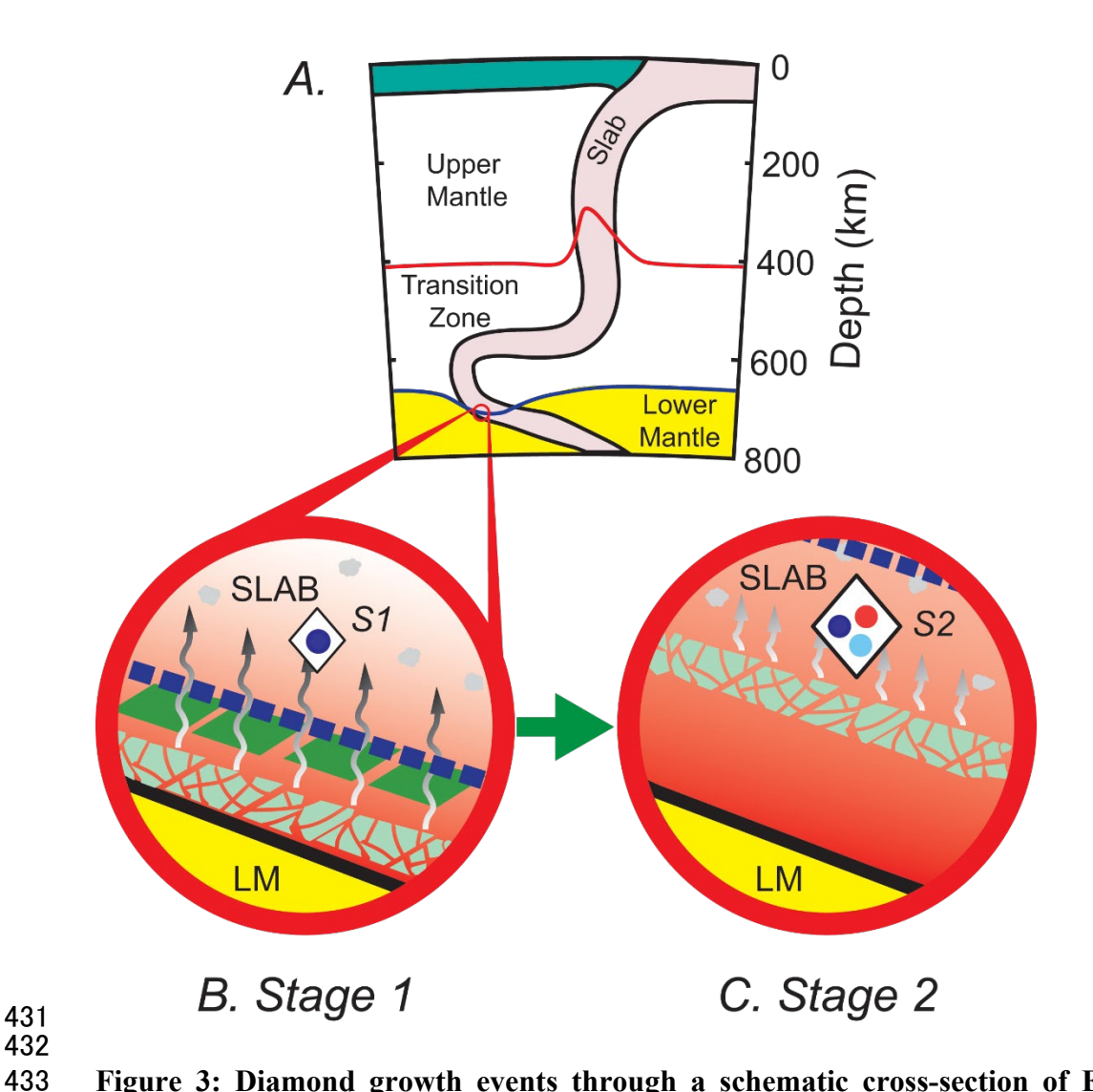


Figure 3: Diamond growth events through a schematic cross-section of Earth, showing subducting slab buckling in the transition zone, such that the slab enters the lower mantle upside down. Figure after [41]. Note that a megalith (a melange of stalled slab at about 660 km depth) would create an equivalent scenario. Red circle indicates region enlarged in (B) and (C). Stage 1: Early in slab warming; dehydration near hot Lower Mantle (LM) – Slab interface (light green crystals). Ascending fluid loses H₂O as new hydrous phases form (dark green crystals). Remaining fluid (darker end of arrows) fractionates to H₂O-poor, reducing CH₄-H₂ compositions by the removal of H₂O. This reduced fluid reacts with ringwoodite, driving it to very Mg-rich composition. Simultaneously, the fluid is precipitating diamond, which encloses a crystal of the high-Mg ringwoodite (blue), isolating it from further reaction. Dark blue dashed line is the position of the ringwoodite (above, cooler) to bridgmanite + ferropericlase (below, warmer) reaction. Stage 2: The slab has continued to warm from below, which drives the ringwoodite to bridgmanite + ferropericlase reaction (dark blue dashed line) upwards into the slab's interior. The warming also causes the dehydration front to sweep upwards into the slab's interior; this dehydration releases H₂O-rich fluid that reacts with iron (small gray blebs) and bridgmanite to precipitate more diamond, which entraps crystals of bridgmanite and ferropericlase as it grows.

435

436

437

438

439 440

441

442

443

444

445

446

447

448

Methods 450 451 *X-ray diffraction* 452 453 Single crystal X-ray diffraction (SCXRD) data were collected at the Department of Geosciences, 454 University of Padova, using a Rigaku Oxford Diffraction SuperNova single-crystal diffractometer, 455 equipped with a Dectris Pilatus 200 K area detector and with a Mova X-ray microsource. A 456 monochromatized Mo $K\alpha$ radiation ($\lambda = 0.71073$ Å), working at 50 kV and 0.8 mA, was used. The 457 original reflection data for olivine in KK203 diamond are reported in the olivine tabb file readable 458 by CrysAlis Pro software (Rigaku Oxford Diffraction) and is deposited open to public at the 459 Research Data University of Padova repository: http://researchdata.cab.unipd.it/id/eprint/652. 460 461 Micro-Raman spectroscopy 462 Raman spectra were collected at the Department of Chemical Sciences, University of Padova, 463 using a Thermo Scientific DXR Raman Microscope with a 532 nm laser. The analyses used a 50× objective with 2.5 cm⁻¹ spectral resolution and 10 mW of power on the sample. The system was 464 465 set at 900 lines/mm grating. 466 467 *X-ray microtomography* 468 Tomography images were collected on beamline 13-BM-D of the GeoSoilEnviro Center for 469 Advanced Radiation Sources (GSECARS), Advanced Photon Source (APS), USA. Collection 470 times with a monochromatic beam with an energy of 28.9 keV were about 15 min⁵⁰. 471 472 Electron probe microanalysis

Electron probe microanalysis of the olivine and enstatite inclusions were collected using a JEOL JXA-8900R with 5 wavelength dispersive spectrometers at the University of Alberta. The beam energy was 20 keV with 30 nA of beam current and 2 μ m diameter. The counting time was 20 s for Si K α , Fe K α , Mn K α , Ni K α , Zn K α , 30 s for V K α , Ti K α , Cr K α , 40 s for Na K α , K K α , Ca K α , Mg K α , and 120 s for Al K α . The olivine with Mg# of 99.90 was rerun using a Cameca SX100 to reduce detection limits and analyse for additional elements. The beam energy was 20 keV with 40 nA of beam current and 5 μ m diameter. The counting time was 60 s for all elements. Electron probe microanalysis of the ferropericlase fragments were collected using a Cameca SX100. The beam energy was 20 keV with 30 nA of beam current and 2 μ m diameter. The counting time was 20 s for all elements.

Mössbauer spectroscopy

Mössbauer spectra were collected on the two largest ferropericlase inclusions after diamond breakage. Spectra were recorded at room temperature in transmission mode on a constant acceleration spectrometer with a nominal 370 MBq 57 Co point source in a 12 μ m thick Rh matrix. The velocity scale was calibrated relative to 25 μ m thick α -Fe foil; line widths of 0.36 mm/s for the outer lines of α -Fe were obtained at room temperature. Spectra were collected for between one and ten days.

Calculation of fo2 for Mg# 99.9 olivine polymorph

Authors^{34,51} predicted that extremely Mg-rich silicates would be stable at conditions more reducing than those of the IW buffer. For example, Fig. 3 of [34] shows that olivine with Mg# 99.9 would

be stable at ~3.5 log units below IW at 10 GPa, coexisting with orthopyroxene, diamond, and a
 FeSiC alloy.

497 At these reducing conditions, the ferrous iron in the silicate is reduced to iron metal:

498
$$Fe_2SiO_4 = 2 Fe + SiO_2 + O_2$$

The equilibrium constant for this reaction is given by:

$$K = \frac{a_{Fe}^2 a_{SiO_2} f_{O_2}}{a_{Fe_2 SiO_4}}$$

And the f_{O2} would be given by:

$$\log f O_2 = \log a_{Fe_2SiO_4} - 2\log a_{Fe} - \log a_{SiO_2} - \Delta_{rxn} G^0 / (2.303RT)$$

The requisite thermodynamic data to calculate the Δ_{rxn} G^0 term were taken from version ds634 of the THERMOCALC database⁵². Quantifying the f_{02} that will stabilize olivine, wadsleyite, or ringwoodite with an Mg# of 99.9 requires values for a_{Fe} for the alloy or melt, and a_{SiO_2} . For the former, we explored a range of possibilities using pure iron as one extreme, as well as activities estimated for the range of metal melt compositions⁵³ following the methodology of [54] and [55]. We tried to constrain a_{SiO_2} by considering a range of possibilities, the most extreme being that pure SiO₂ might precipitate in the reaction in a localized environment. We also considered two possible reactions that might be appropriate for defining the a_{SiO_2} :

511
$$2 \text{ Mg}_2\text{SiO}_4 + 2 \text{ SiO}_2 = \text{Mg}_3(\text{MgSi})\text{Si}_3\text{O}_{12} \text{ (majorite)}$$

$$Mg_2SiO_4 = 2 MgO (ferropericlase) + SiO_2$$

In turn, these required assumptions regarding possible compositions of the majorite for the first reaction and the ferropericlase for the second. We explored a range of possibilities at conditions of 10, 15, and 20 GPa, at temperatures of 1,200°, 1,400°, and 1,800°C as detailed in Supplementary

- Table 3. This range of pressures spanned the stabilities of olivine (10 GPa), wadsleyite (15 GPa)
- and ringwoodite (20 GPa). We used the solution models of [35] for olivine, wadsleyite,
- 518 ringwoodite, and ferropericlase in our calculations, supplemented by an ideal solution model for
- 519 majorite.
- As shown in Extended Data Figure 3, these calculations produce a range of possible conditions
- from ~4 to ~6.7 log units lower than the IW buffer curve, essentially independent of temperature
- or pressure. The latter implies the polymorph of (Mg,Fe)₂SiO₄ does not have a significant influence
- on these results. In all cases, the " \star " is the result for pure iron and pure SiO₂.
- 524 Data availability: The original reflection data for olivine in KK203 diamond,
- 525 Supplementary Table 1, Table 2 and Table 3 were deposited with the EarthChem as:
- Nestola, F., Regier, M., Luth, R. W., Pearson, D. G., Stachel, T., McCammon, C. A., Wenz, M.
- W., Jacobsen, S. D., Anzolini, C., Bindi, L., Harris, J. W., 2022. Experimental and calculation data
- 528 KK203 diamond, Version 1.0. Interdisciplinary Earth Data Alliance (IEDA).
- 529 http://doi.org/10.26022/IEDA/112541.

References cited only in the Methods section

- 533 50. Wenz, M. D. et al. Fast identification of mineral inclusions in diamond at GSECARS using synchrotron X-ray microtomography, radiography and diffraction. *J. Synchrotron Radiat.* 26,
- 535 1763–1768 (2019).

530 531

532

536

540

544

548

- 51. Golubkova, A., Schmidt, M.W. & Connolly, J.A.D. Ultra-reducing conditions in average
- mantle peridotites and in podiform chromitites: a thermodynamic model for moissanite (SiC)
- 539 formation. *Contrib. Mineral. Petr.* **171**, art. n. 41 (2016).
- 541 52. Holland, T.J.B. & Powell, R. An improved and extended internally consistent thermodynamic
- dataset for phases of petrological interest, involving a new equation of state for solids. J.
- 543 *Metamorph. Geol.* 29, 333–383 (2011).
- 53. Smith, E.M., Ni, P., Shirey, S.B., Richardson, S.H., Wang, W. & Shahar, A. Heavy iron in
- large gem diamonds traces deep subduction of serpentinized ocean floor. Sci. Adv. 7, eabe9773
- 547 (2021).
- 549 54. Fichtner, C.E., Schmidt, M.W., Liebske, C., Bouvier, A.S. & Baumgartner, L.P. Carbon
- partitioning between metal and silicate melts during Earth accretion. Earth Planet. Sc. Lett. 554.
- 551 116659 (2021).

55. Wade, J. & Wood, B.J. Core formation and the oxidation state of the Earth. *Earth Planet. Sc. Lett.* **236**, 78–95 (2005).

Acknowledgments: This research used resources of the Advanced Photon Source, a U.S. Department of Energy (DOE) Office of Science User Facility operated for the DOE Office of Science by Argonne National Laboratory under Contract No. DE-AC02-06CH11357. We acknowledge the support of GeoSoilEnviroCARS (Sector 13), which is supported by the U.S. National Science Foundation (NSF) - Earth Sciences (EAR-1128799), and the Department of Energy, Geosciences (DE-FG02-94ER14466) and staff scientists Matt Newville, Tony Lanzirotti and Mark Rivers. S.D.J. acknowledges support from NSF grant EAR-1853521. NSERC Discovery grants to Luth, Pearson and Stachel funded aspects of this research. The authors acknowledge Arno Rohrbach and an anonymous reviewer for very valuable comments that prompted a re-think of our fo2 estimate and formation model.

Author contributions: M.E.R., C.A. and F.N. collected and interpreted the XRD data. M.E.R. characterized the inclusions by EPMA and Raman spectroscopy. F.N. and M.E.R. wrote original manuscript. R.W.L. and T.S. developed the diamond growth model. F.N. performed the geobarometric calculations on olivine. C.M. characterized the inclusions by Mössbauer spectroscopy. M.D.W, M.E.R, and S.D.J. conducted tomographic image collection and analyses. R.W.L. and M.E.R. did the f_{02} calculations. J.W.H. provided the diamond and helped describe and break the sample All co-authors improved interpretations and provided editing.

Table 1. Electron Probe Microanalyses for inclusions in diamond KK203. All values are average analyses (ox wt% = oxide weight %; a.p.f.u. = atoms per formula unit).

	Ferropericlase*		Olivine		Enstatite*		High-Ca pyroxene		
	ox wt%	a.p.f.u.	ox wt%	a.p.f.u.	ox wt%	a.p.f.u.	ox wt%	a.p.f.u.	
SiO ₂	bdl	bdl	42.12	0.998	57.56	1.971	50.69	1.858	
TiO ₂	bdl	bdl	bdl	bdl	bdl	bdl	0.13	0.004	
Al_2O_3	bdl	bdl	bdl	bdl	0.32	0.013	7.63	0.330	
Cr ₂ O ₃	0.30	0.002	bdl	bdl	0.38	0.010	0.60	0.017	
FeO	20.98	0.131	0.10	0.002	2.68	0.077	2.57	0.079	
NiO	1.33	0.008	bdl	bdl	bdl	bdl	0.05	0.002	
MnO	0.17	0.001	0.02	0.000	0.10	0.003	0.09	0.003	
MgO	76.69	0.857	56.64	2.001	38.01	1.940	14.96	0.818	
CaO	bdl	bdl	bdl	bdl	0.08	0.003	20.68	0.812	
Na ₂ O	0.04	0.001	bdl	bdl	0.02	0.001	1.19	0.038	
Total	99.51	1.000	98.88	3.001	99.15	4.018	98.59	3.961	
Mg#	86.7		99.90		96.2		91.2		

*average of multiple fragments; bdl = below detection limit. High-Ca pyroxene is zoned and therefore likely represents a non-primary, reacted multi-mineralic phase. ZnO, V_2O_3 , and K_2O were analysed in all inclusions, plus Co, Cu, and P in olivine, but all were below detection limit. P was also checked for ferropericlase but it was below the detection limit.

Extended Data Figure 1. Raman spectrum of enstatite measured in diamond KK203 (in blue solid line). Reference spectrum of enstatite is in solid red line (RRUFF ID: R070641). The data reduction software is OMNIC 9 (Thermo Fisher Scientific Inc.). Extended Data Figure 2. X-ray tomographic image of KK203, collected at GSECARS, showing no cracks leading to inclusions. Entire diamond could not fit into field of view. Extended Data Figure 3. Calculated values of log fo2 relative to the IW buffer at 10, 15, and 20 GPa and 1200, 1400, and 1800°C necessary to stabilize a (Mg,Fe)₂SiO₄ polymorph with Mg# = 99.9. The different values at each condition reflect the range of assumed activities of Fe and SiO₂ (see text for details). The stars denote the case with both activities equal to one. See tabulated values in the accompanying spreadsheet for details of the calculations. Extended Data Table 1. Hyperfine parameters of ferropericlase from KK203 determined from room temperature Mössbauer spectrum.